



# Extension of the Electron Diffusion Region in a Guide Field Magnetic Reconnection at Magnetopause

Z. H. Zhong<sup>1</sup> , M. Zhou<sup>1</sup>, R. X. Tang<sup>1</sup>, X. H. Deng<sup>1</sup>, Y. V. Khotyaintsev<sup>2</sup> , B. L. Giles<sup>3</sup>, W. R. Paterson<sup>3</sup>, Y. Pang<sup>1</sup>, H. Y. Man<sup>1</sup>,  
C. T. Russell<sup>4</sup> , and J. L. Burch<sup>5</sup>

<sup>1</sup>Nanchang University, Nanchang 330031, People's Republic of China; [monmomentum82@gmail.com](mailto:monmomentum82@gmail.com)

<sup>2</sup>Swedish Institute of Space Physics, Uppsala SE-75121, Sweden

<sup>3</sup>NASA, Goddard Space Flight Center, Greenbelt, MD, USA

<sup>4</sup>Department of Earth, Planetary, and Space Sciences, UCLA, Los Angeles, CA, USA

<sup>5</sup>Southwest Research Institute, San Antonio, TX, USA

Received 2019 December 7; revised 2020 February 12; accepted 2020 February 29; published 2020 March 19

## Abstract

The structure of the electron diffusion region (EDR) in different plasma regimes is an outstanding question related to magnetic reconnection. Here we report a long EDR that extended at least 20 ion inertial lengths downstream of an  $X$  line at the Earth's magnetopause, which was observed by the Magnetospheric Multiscale mission. This EDR was detected in the exhaust of an asymmetric magnetic reconnection with a moderate guide field, the reconnection rate of which was  $\sim 0.1$ . It corresponds to strong positive energy dissipation ( $J \cdot E' > 0$ ) and enhancement of electron nongyrotropy. The energy dissipation was contributed by the electron jet and non-ideal electric field along the outflow direction, which suggests that the EDR probably plays more important roles in the energy conversion in magnetic reconnection than previously thought. Our result could be a significant step toward fully understanding the structure of the EDR.

*Unified Astronomy Thesaurus concepts:* [Solar magnetic reconnection \(1504\)](#); [Plasma physics \(2089\)](#); [Space plasmas \(1544\)](#); [Planetary boundary layers \(1245\)](#)

## 1. Introduction

One of the most important energy release processes in laboratory and astrophysical plasma is magnetic reconnection, which efficiently converts magnetic energy into plasma energy during the reconfiguration of magnetic field lines. It is currently believed that magnetic reconnection is initiated in a small-scale diffusion region and then develops to a macroscopic scale. The fast collisionless reconnection model shows that the diffusion region is a nested two-scale structure due to the different masses of ions and electrons (e.g., Birn et al. 2001). Ions decouple from the magnetic field ( $E + v_i \times B \neq 0$ ) in the ion diffusion region (IDR) where Hall effect is important (Deng & Matsumoto 2001; Øieroset et al. 2001; Drake et al. 2008; Zhou et al. 2009, 2017; Eastwood et al. 2010a). Electrons decouple from the magnetic field ( $E + v_e \times B \neq 0$ ) in the electron diffusion region (EDR), which is embedded within the IDR.

Recently it was found that the EDR defined by  $E + v_e \times B \neq 0$  consists of the inner EDR and the outer EDR in anti-parallel reconnection (Daughton et al. 2006; Fujimoto 2006; Karimabadi et al. 2007; Shay et al. 2007; Zenitani et al. 2011; Hwang et al. 2017). The inner EDR is several ion inertial lengths along the outflow direction (Karimabadi et al. 2013). It wraps the  $X$  line and features intense out-of-plane current density, non-ideal electric field  $E + v_e \times B \neq 0$ , electron nongyrotropy, and energy dissipation with  $J \cdot E' = J \cdot (E + v_e \times B) > 0$  (Burch et al. 2016b; Zhou et al. 2019; Zhong et al. 2018, 2019). The outer EDR can extend tens of ion inertial lengths ( $d_i$ ) away from the  $X$  line (Phan et al. 2007; Shay et al. 2007; Zhou et al. 2014). It is manifested as a super-Alfvénic electron jet that outruns the moving magnetic field. This results in the deceleration of the super-Alfvénic electron jet and  $J \cdot E' < 0$ . Although the outer EDR is a non-ideal region ( $E + v_e \times B \neq 0$ ), it does not contribute to positive magnetic energy dissipation or control

the reconnection rate, which contrasts with the inner EDR (Zenitani et al. 2011; Nakamura et al. 2018).

Goldman et al. (2011) pointed out that a weak guide field would destroy the outer EDR. Le et al. (2013) found that the structure of the EDR depends on the strength of the guide field and the inflow plasma  $\beta$ . They identified extended magnetized electron jets in the exhaust in the presence of a moderate guide field. This jet is driven by electron pressure anisotropy in the exhaust (Egedal et al. 2013; Le et al. 2013, 2019).

The above studies are related to reconnection with symmetric inflow boundaries. Recently, an outer EDR has been identified in asymmetric reconnection without guide field (Hwang et al. 2017). However, the effect of guide field on the structure of the EDR in asymmetric reconnection is unclear. Here we report a novel observation by *Magnetospheric Multiscale* (*MMS*) mission (Burch et al. 2016a) showing that an electron jet extended at least  $20 d_i$  away from the  $X$  line in the exhaust of an asymmetric reconnection with a moderate guide field. The electron jet bore similar features to the standard EDR, where the electron frozen-in condition is violated and magnetic energy is dissipated. The *MMS* data used in this study are from the following instruments: the Fluxgate Magnetometer (Russell et al. 2016), the Fast Plasma Investigation (Pollock et al. 2016), and the Electric Double Probe (Lindqvist et al. 2016; Ergun et al. 2016).

## 2. Event Overview

Figure 1 presents the *MMS*1 spacecraft measurements during 01:35–02:10 UT on 2015 December 13, when it was around  $[10.5, -3.9, -1.1] R_E$  in Geocentric Solar Magnetospheric (GSM) coordinates. Four *MMS* spacecraft formed a regular tetrahedron in space with an average spacing of 16 km. *MMS* was in the low latitude boundary layer during almost the entire time interval in Figure 1 since the magnetospheric and

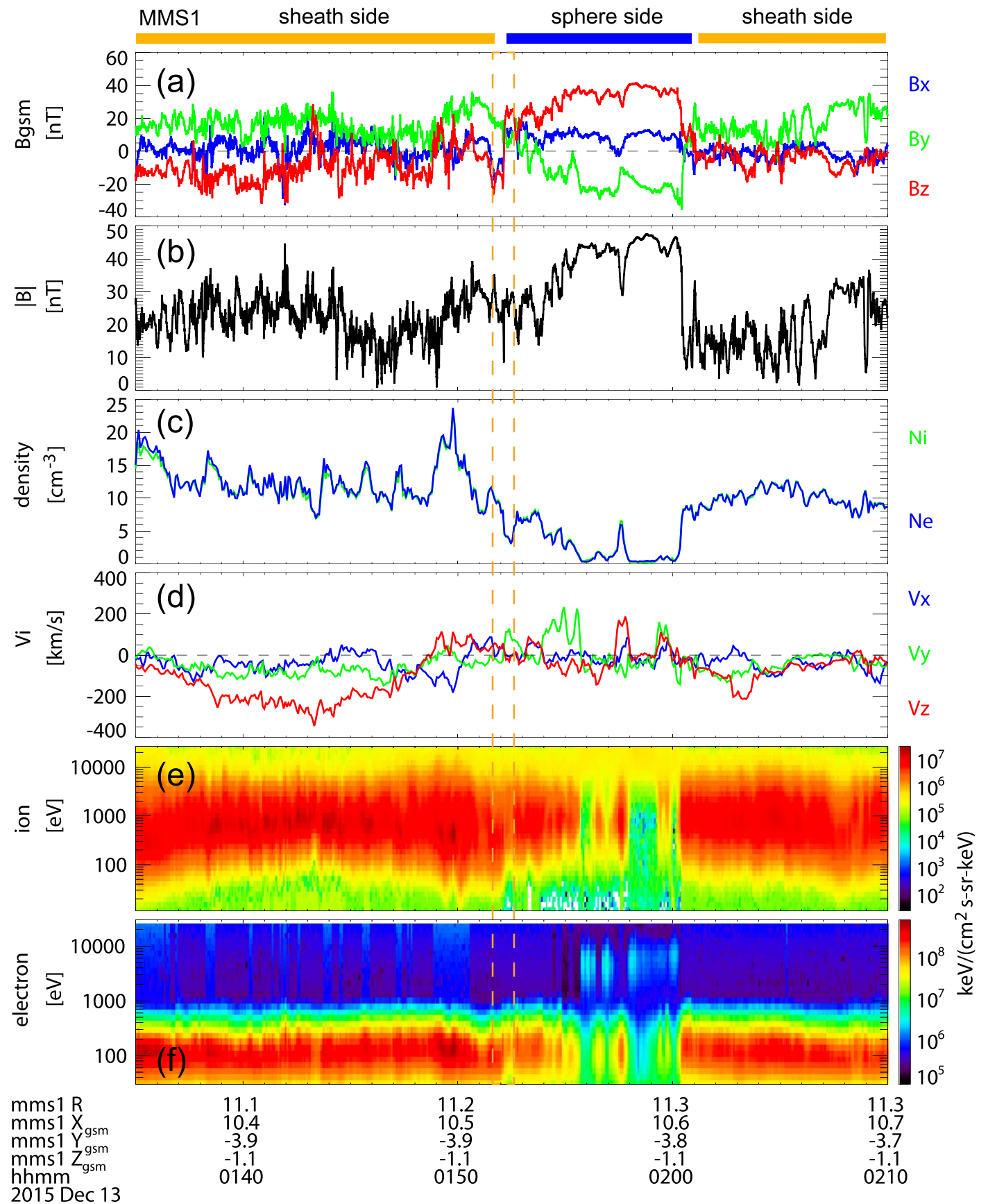


**Figure 1.** Overview of *MMS1* observations between 01:35 and 02:10 UT on 2015 December 13. From the top to the bottom are: (a) three components of the magnetic field; (b) total magnetic field; (c) ion and electron density; (d) three components of the ion bulk flow; (e) ion and (f) electron differential energy fluxes. All the vectors are presented in GSM coordinates.

magnetosheath plasmas were mixed (Figures 1(e) and (f)). It crossed the magnetopause current sheet from the magnetosheath side (characterized by the high plasma density and turbulent magnetic fields with  $B_z < 0$ ) to the magnetospheric side (characterized by the low plasma density and less turbulent magnetic field with  $B_z > 0$ ) at around 01:52 UT, and returned to the magnetosheath side at around 02:01 UT. A southward ion flow (near  $-350 \text{ km s}^{-1}$ ) was observed by *MMS1* in the magnetosheath side from 01:43 UT (Figure 1(d)). The flow was relatively weaker in the magnetospheric side and changed directions a few times during the current sheet crossing. Here we focus on the first current sheet crossing (marked by the orange dashed box in Figure 1).

### 3. The Extended EDR in a Hall Region

Figure 2 shows the four spacecraft observations of the current sheet crossing around 01:52 UT in the local boundary normal (LMN) coordinates, where  $N$  points sunward along the current sheet normal,  $L$  is the maximum variation direction that points along the reconnecting magnetic field component, and  $M$  completes a right-handed orthogonal coordinate system, i.e.,  $M = N \times L$ . The transformation from GSM to LMN coordinates, which was obtained by the minimum variance analysis (MVA; Sonnerup & Scheible 1998) based on the magnetic field observed by *MMS1* between 01:51:58 and 01:52:22 UT, is  $L = [0.435, -0.125, 0.892]$ ,  $M = [-0.290, -0.957, 0.008]$ , and  $N = [0.852, -0.262, -0.453]$ . The medium-to-minimum (maximum-to-medium) eigenvalue ratio is  $\sim 17$  (18), indicating a reliable LMN coordinate system inferred from MVA (Lepping & Behannon 1980).

The four *MMS* spacecraft observed similar features of this current sheet. The magnetic field  $B_L$  reversed from about  $-22$ – $22$  nT (the vertical purple line in Figure 2(a) marks the  $B_L = 0$ ), which suggests that *MMS* crossed the current sheet from the magnetosheath side to the magnetospheric side. The normal speed of this current sheet was estimated as  $\sim 45 \text{ km s}^{-1}$  by the multi-spacecraft timing method (Schwartz 1998) based on the reference point  $B_L = 0$ . This normal is only  $6^\circ$  different from the normal estimated by the MVA, which implies that the derived current sheet normal is reliable. The shear angle between the asymptotic magnetic fields on the two sides of the current sheet was about  $123^\circ$ , corresponding to a guide field  $B_g \sim -12 \text{ nT} \sim -0.55 B_0$ ; here,  $B_0 \sim 22 \text{ nT}$  is the asymptotic magnetic field.

Figure 2(e) displays that the asymmetric plasma density was  $\sim 9 \text{ cm}^{-3}$  in the high-density side (magnetosheath side) and was  $\sim 4 \text{ cm}^{-3}$  in the low-density side (magnetospheric side). Plasma density has a dip ( $\sim 6 \text{ cm}^{-3}$ ) around the magnetosheath side separatrix, consistent with previous reports (Khotyaintsev et al. 2006; Zhou et al. 2011). The ion bulk flow  $V_{iL}$  (Figure 2(f)) exhibits a small enhancement with a peak speed  $\sim 80 \text{ km s}^{-1}$  at the center of the current sheet (note that the background velocity was about  $50 \text{ km s}^{-1}$  in the magnetosheath side), while it reverses to negative in the magnetospheric side, consistent with the sign change of the electron bulk flow  $V_{eL}$  (Figure 2(g)). The reconnected magnetic field  $B_N$  (Figure 2(c)) was negative during the plotted interval. Therefore, we conclude that *MMS* crossed a reconnecting current sheet on the  $+L$  side of the  $X$  line as illustrated in Figure 3.

Figure 2(b) presents that the magnetic field  $B_M$  exhibits a bipolar variation superposed on the guide field  $B_g$ . The polarity change of  $B_M$  is consistent with the predicted Hall out-of-plane

magnetic field in collisionless reconnection. The bipolar variation of  $B_M$  was associated with a tripolar variation (positive-negative-positive) of the current density  $J_L$  (Figure 2(d)). The two positive  $J_L$  were located away from the current sheet where  $|B_L|$  was around 20 nT, while the negative  $J_L$  was at the center of the current sheet. The current directions are consistent with the variation of  $B_M$  according to the Ampere's law, thus the tripolar current structure formed a Hall current loop, as depicted in Figure 3. Moreover, this Hall current loop was primarily attributed to the electron bulk flow  $V_{eL}$  (Figure 2(g)). This implies that the two electron bulk flows along  $-L$  around the separatrices were the electron inflow, while the electron bulk flow along  $+L$  within the current sheet was the reconnection outflow. The edges of Hall magnetic field (marked by the two vertical orange lines in Figure 2) were the locations of the two separatrices.

It has been suggested that the Hall magnetic fields are distorted with respect to the reconnecting current sheet in both the guide field reconnection and asymmetric reconnection (Pritchett 2008; Eastwood et al. 2010b; Zhou et al. 2018). We notice that the Hall magnetic field was nearly symmetric across this current sheet. This is probably due to the fact that the effect of the density asymmetry counter-balanced the effect of the guide field. This is because the imposed guide field in  $-M$  tends to reduce the Hall  $B$  field on the sheath side, while the density asymmetry will enhance the Hall  $B$  field on the sheath side (Pritchett & Mozer 2009; Chen et al. 2017). Thus, the diffusion region is quasi-symmetric, as is depicted in Figure 3.

The width of this Hall region along the current sheet normal was  $\sim 45 \text{ km s}^{-1} * 9.5 \text{ s} \sim 420 \text{ km} \sim 5.6 d_i$  (ion inertial length,  $1 d_i \sim 76 \text{ km}$ , given the ion density  $\sim 9 \text{ cm}^{-3}$  on the magnetosheath side). We assume that the separatrices were straight lines originating from the  $X$  line, and the magnetic field lines in the reconnection plane ( $L$ - $N$  plane) around the separatrices were parallel to the separatrices. According to the geometry relation of similar triangles, we obtain the cone angle  $\theta$  as follows:

$$\tan \theta \sim \delta/D \sim B_N/B_L \quad (1)$$

where  $\delta$  ( $2\delta \approx 5.6 d_i$ ) is the half-width of the exhaust determined by *MMS*,  $D$  is the distance between the  $X$  line and *MMS* when it was in the central current sheet.  $B_N$  and  $B_L$  were magnetic fields at the separatrices. The values of  $B_N$  and  $B_L$  have been averaged around the two separatrices (01:52:04–01:52:05 UT and 01:52:13–01:52:14 UT, respectively). The estimated cone angle  $\theta$  was about  $8^\circ$  for both separatrices. Knowing the half-width of the Hall region  $\sim 2.8 d_i$  and the cone angle  $\sim 8^\circ$ , we infer that this current sheet crossing occurred at about  $1500 \text{ km} \sim 20 d_i$  downstream of the  $X$  line, which is diagrammatized in Figure 3. Furthermore, the dimensionless reconnection rate can be calculated by the equation given in Liu et al. (2017) and Nakamura et al. (2018) based on the cone angle of the separatrix:

$$R \approx \frac{E_r}{V_{Ai} B_b} \approx \tan \theta \left( \frac{1 - \tan^2 \theta}{1 + \tan^2 \theta} \right)^2 \sqrt{1 - \tan^2 \theta} \quad (2)$$

We get the dimensionless reconnection rate  $R \sim 0.13$ , which is in accordance with previous simulations and observations (Xiao et al. 2007; Liu et al. 2017).

Figure 4 details the electron jet within the current sheet. Figure 4(b) shows the electron bulk velocity observed by *MMS1*

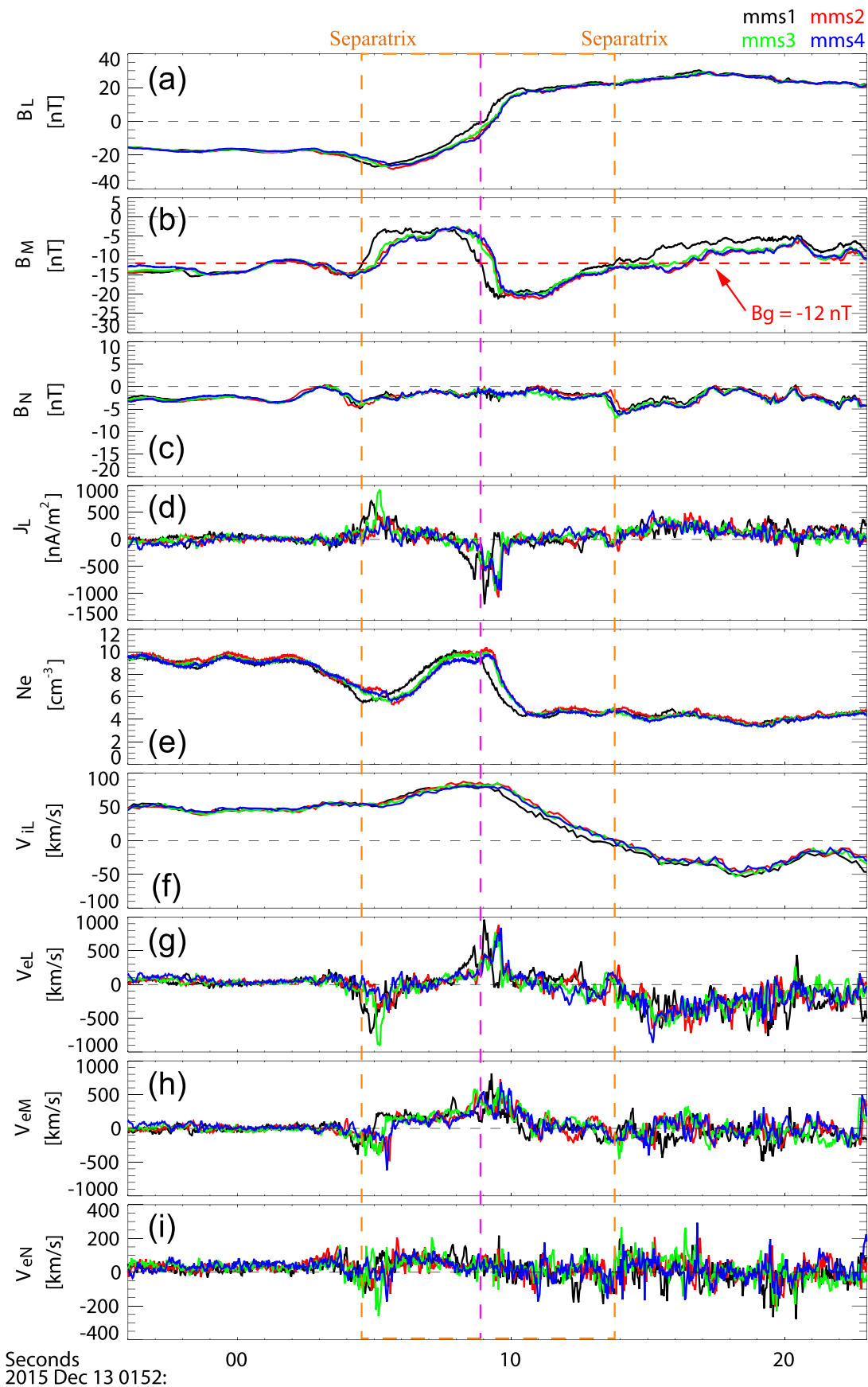


**Figure 2.** Four spacecraft observations of the reconnecting current sheet. (a) Magnetic field  $B_L$ , (b)  $B_M$  and (c)  $B_N$ ; (d)  $L$  component of the electric current density calculated from the plasma density and bulk velocity, i.e.,  $J = ne(v_i - v_e)$ ; (e) electron density; (f)  $L$  component of the ion bulk flow; (g)–(i) electron bulk flow  $v_{eL}$ ,  $v_{eM}$ , and  $v_{eN}$ , respectively. The orange box marks the Hall region, and the purple dashed line marks the center of the current sheet where  $B_L = 0$ . All the vectors are presented in the LMN coordinate system.

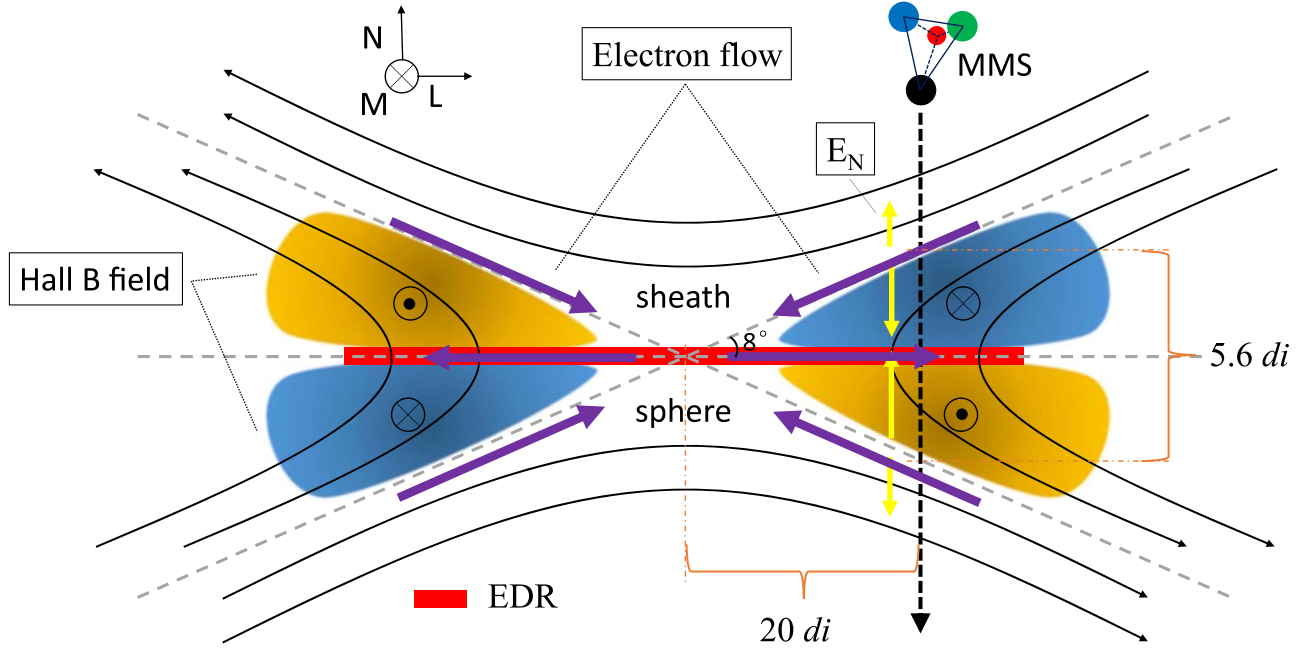


**Figure 3.** 2D view of this reconnection layer in the  $L$ - $N$  plane. *MMS* (denoted by the black dashed arrow) crossed the extended EDR (denoted by the red bar) in the reconnection exhaust along the  $-N$  direction, during which *MMS* detected the inflowing and outflowing electrons (denoted by the purple arrows), and the Hall electric field  $E_N$  (denoted by the yellow arrows). The blue and orange shades represent the Hall magnetic field. The open angle of the separatrices was  $\sim 8^\circ$ . The width of the Hall region was  $5.6 d_i$ , while the distance between the  $X$  line and the crossing point of *MMS* and the EDR was  $\sim 20 d_i$ .

in LMN coordinates. The width of the positive  $V_{eL}$  enhancement was about  $70 \text{ km} \sim 0.9 d_i$  (during 01:52:08.9–01:52:09.5 UT), while the width of the positive  $V_{eM}$  enhancement was about  $160 \text{ km} \sim 2 d_i$  (during 01:52:07–01:52:10.5 UT). Both  $V_{eL}$  and  $V_{eM}$  exhibit bifurcated structure, that is, a dip between the two peaks. The two peaks of  $V_{eL}$  were not coincident with the two peaks in  $V_{eM}$ . The peak speed of the first  $V_{eL}$  enhancement was about  $600 \text{ km s}^{-1}$ , while the peak speed of the second one was up to  $1000 \text{ km s}^{-1}$ . Bifurcated out-of-plane and outward electron flows have both been observed in the EDR (Burch & Phan 2016; Hwang et al. 2017).

Figures 4(d)–(f) show the three components of the electric field. The ion convective electric fields (blue curves) were different from the measured electric fields (black curves) within the Hall region, i.e.,  $E + v_i \times B \neq 0$ , indicating the decoupling of ions from the magnetic field. In contrast, the electron convective electric fields (red curves) balance the measured electric fields, i.e.,  $E + v_e \times B = 0$ , during the whole plotted interval, except in the electron outflow jet where there were evident differences between the negative electric field  $E_L$  and the nearly zero  $-(v_e \times B)_L$  (Figure 4(d)). This implies that electron frozen-in condition was violated within the electron jet. The non-ideal electric fields ( $E + v_e \times B \neq 0$ ) were coincident with the two electron outflow jets and led to energy dissipation  $J \cdot E' > 0$  at the two jets (Figures 4(g) and (h)). The energy dissipation caused by super-Alfvénic electron jets has been observed within the IDR with proximity to the  $X$  line of magnetosheath reconnection (Wilder et al. 2017, 2018) and tailward flow burst in magnetotail (Chen et al. 2019).

The peaks of the non-ideal electric fields were about  $-2 \text{ mV m}^{-1}$ , and the peak  $J \cdot E'$  for the first electron outflow jet was  $\sim 1.4 \text{ nW m}^{-3}$  and for the second one was  $\sim 2.7 \text{ nW m}^{-3}$ . The width of the energy dissipation layer corresponding to the second electron outflow jet was about  $0.18 d_i \sim 8 d_e$  (electron inertial length,  $1 d_e \sim 1.8 \text{ km}$ ). Figure 4(h) illustrates that the

energy dissipation was mainly attributed to the current and electric field perpendicular to the magnetic field. This is different from previous observations of reconnection with guide field, where energy dissipation was mainly due to parallel electric field (Wilder et al. 2017, 2018; Zhou et al. 2019). The electric field  $E_N$  exhibits a quadrupolar variation across the current sheet. The measured  $E_N$  was the Hall electric field because it was largely balanced by the electron convective electric field  $-(v_e \times B)_N$ .

The measure of the electron nongyrotropy  $Q^{0.5}$  (Swisdak 2016) also exhibits a peak of about 0.06 corresponding to the second electron jet (Figure 4(i)). The peak values of  $J \cdot E'$  and  $Q^{0.5}$  are close to the median values of these parameters of the EDRs observed by *MMS* at the dayside magnetopause (Webster et al. 2018). Figure 4(k) shows the 2D electron velocity distributions at the second electron jet. An obvious crescent-shaped structure in the plane perpendicular to the magnetic field was observed. This type of electron velocity distribution has frequently been found around electron-scale field reverse layers and is a typical signature of the EDR (Burch et al. 2016b; Lapenta et al. 2017). In addition, parallel and anti-parallel drifting electrons around the two separatrices are seen in the electron velocity distributions in Figures 4(j) and (l). These electrons show small enhancement of the nongyrotropy. They represent the inflowing population and contributed to the electron flow that bounded the Hall region.

#### 4. Discussion and Summary

The electron outflow jet reported here corresponded to a positive energy dissipation, hence it was different to the super-Alfvénic electron jet (the outer EDR) in anti-parallel reconnection, which is characterized by  $J \cdot E' < 0$  (Karimabadi et al. 2007; Zenitani et al. 2011; Hwang et al. 2017; Nakamura et al. 2018). On the contrary, it involved a few essential features of

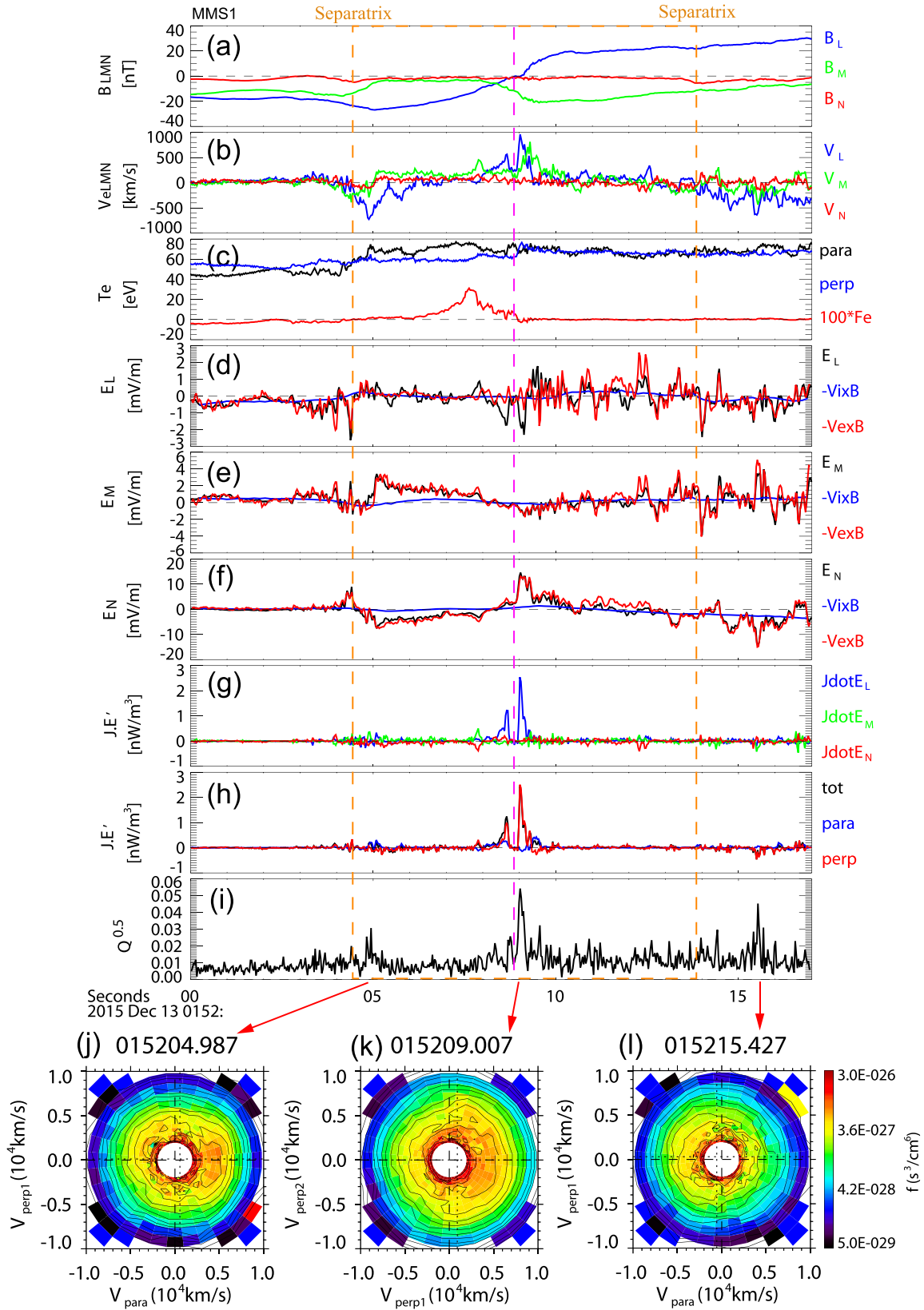


**Figure 4.** Features of the electron jets within the current sheet observed by *MMS1*. (a) Three components of the magnetic field; (b) electron bulk flow; (c) parallel (black) and perpendicular (blue) electron temperature and firehose instability parameter  $F_e = \mu_0(P_{e\parallel} - P_{e\perp})/B^2$  (the red curve represents  $100F_e$ ), (d)–(f) three components of the measured electric field (black),  $-(\mathbf{v}_\perp \times \mathbf{B})$  (blue) and  $-(\mathbf{v}_\parallel \times \mathbf{B})$  (red); (g) decomposition of the energy dissipation into three components  $J_\perp E'_L$  (blue),  $J_\parallel E'_M$  (green) and  $J_\perp E'_N$  (red); (h)  $\mathbf{J} \cdot \mathbf{E}'_{\text{tot}}$  (black),  $J_\parallel E'_L$  (blue) and  $J_\perp E'_N$  (red); (i) electron nongyrotropy; (j)–(l) 2D cuts of  $V_{\text{para}}-V_{\text{perp1}}$ ,  $V_{\text{perp1}}-V_{\text{perp2}}$  and  $V_{\text{para}}-V_{\text{perp1}}$  of the 3D electron velocity distributions at the times denoted by the three red arrows.  $V_{\text{perp1}}$  is defined as  $(\mathbf{b} \times \mathbf{v}) \times \mathbf{b}$ , and  $V_{\text{perp2}}$  is defined as  $\mathbf{b} \times \mathbf{v}$ , where  $\mathbf{b}$  and  $\mathbf{v}$  are the unit vector of the magnetic field and the electron bulk velocity, respectively.

the inner EDR close to  $X$  line, such as  $J \cdot E' > 0$  and electron nongyrotropy.




The Hall reconnection model suggests that the length of the EDR is on the electron-scale and thus the EDR does not form a bottleneck to the fast reconnection (Karimabadi et al. 2013; Liu et al. 2018). Here we find that the aspect ratio of this EDR was quite small ( $< 0.09 d_i / 20 d_i \approx 0.0045$ , where  $0.09 d_i$  was the half-width of the EDR and  $20 d_i$  was the minimum length of the EDR on the one side of the  $X$  line), however, the reconnection remained fast as the inferred reconnection rate was 0.13. The discrepancy between the fast reconnection rate and small aspect ratio of this EDR suggests that this extended EDR did not control the reconnection rate, equivalently, there was no electron inflow into this extended EDR. Therefore, it was not the inner EDR seen in the anti-parallel reconnection.

It was also different from the extended electron jet embedded within the ion exhaust in the presence of guide field (Le et al. 2013, 2019). Figure 4(c) presents the parallel (black) and perpendicular (blue) electron temperature, and electron fluid firehose parameter  $F_e = \mu_0(P_{e\parallel} - P_{e\perp})/B^2$  (red), where  $\mu_0$  is the permeability of free space,  $P_{e\parallel}$  and  $P_{e\perp}$  is the parallel and perpendicular electron pressure, respectively. We see that the electron anisotropy and  $F_e$  ( $< 0.1$ ) are very small at this EDR. This indicates that the extended current layer was not driven by electron pressure anisotropy in the exhaust, which is distinct from previous simulations (Le et al. 2013, 2019). Kinetic simulations with asymmetry boundary and guide field are required to understand the nature of this EDR.

In summary, an elongated EDR was observed at  $\sim 20 d_i$  downstream of the  $X$  line in the asymmetric magnetic reconnection with a moderate guide field. The EDR was featured by intense magnetic energy dissipation, electron nongyrotropy and super-Alfvénic electron jet. The width of this EDR along the current sheet normal was  $\sim 8 d_e$ . The dissipating electron jet provides a further channel for energy dissipation beyond the electron-scale region around the reconnection site. Because the volume of this dissipating electron jet is much larger than the localized EDR from previous studies (Hesse & Winske 1998; Mozer et al. 2002; Zenitani et al. 2011; Torbert et al. 2018), the EDR probably contributes more to the overall energy dissipation in reconnection than previously thought. This long ( $> 20 d_i$ ) EDR has not been found in previous observations and simulations, hence posing a new view of the structure of the EDR in asymmetric reconnection, which deserves further investigation from both simulations and observations.

We thank the entire *MMS* team and *MMS* Science Data Center for providing the high-quality data for this study. This work was supported by National Natural Science Foundation of China (NSFC) under grant Nos. 41674144 and 41774154. Data used for this study are publicly available from the *MMS* Science Data Center (<https://lasp.colorado.edu/mms/sdc/public/>).

## ORCID iDs

Z. H. Zhong  <https://orcid.org/0000-0003-0617-4418>  
 Y. V. Khotyaintsev  <https://orcid.org/0000-0001-5550-3113>  
 C. T. Russell  <https://orcid.org/0000-0003-1639-8298>

## References

- Birn, J., Drake, J. F., Shay, M. A., et al. 2001, *JGR*, 106, 3715  
 Burch, J. L., Moore, T. E., Torbert, R. B., et al. 2016a, *SSRv*, 199, 5  
 Burch, J. L., & Phan, T. D. 2016, *GeoRL*, 43, 8327  
 Burch, J. L., Torbert, R. B., Phan, T. D., et al. 2016b, *Sci*, 352, aaf2939  
 Chen, L. J., Hesse, M., Wang, S., et al. 2017, *JGRA*, 122, 5235  
 Chen, Z. Z., Fu, H. S., Liu, C. M., et al. 2019, *GeoRL*, 46, 5698  
 Daughton, W., Scudder, J., & Karimabadi, H. 2006, *PhPI*, 13, 072101  
 Deng, X. H., & Matsumoto, H. 2001, *Natur*, 410, 557  
 Drake, J. F., Shay, M. A., & Swisdak, M. 2008, *PhPI*, 15, 042306  
 Eastwood, J. P., Phan, T. D., Øieroset, M., et al. 2010a, *JGRA*, 115, A08215  
 Eastwood, J. P., Shay, M. A., Phan, T. D., et al. 2010b, *PhRvL*, 104, 205001  
 Egedal, J., Le, A., & Daughton, W. 2013, *PhPI*, 20, 061201  
 Ergun, R. E., Tucker, S., Westfall, J., et al. 2016, *SSRv*, 199, 167  
 Fujimoto, K. 2006, *PhPI*, 13, 072904  
 Goldman, M. V., Lapenta, G., Newman, D. L., et al. 2011, *PhRvL*, 107, 135001  
 Hesse, M., & Winske, D. 1998, *JGR*, 103, 26479  
 Hwang, K. J., Sibeck, D. G., Choi, E., et al. 2017, *GeoRL*, 44, 2049  
 Karimabadi, H., Daughton, W., & Scudder, J. 2007, *GeoRL*, 34, L13104  
 Karimabadi, H., Roytershteyn, V., Daughton, W., et al. 2013, in *Microphysics of Cosmic Plasmas*, ed. A. Balogh et al. (Boston, MA: Springer), 231  
 Khotyaintsev, Y. V., Vaivads, A., Retinò, A., et al. 2006, *PhRvL*, 97, 205003  
 Lapenta, G., Berchem, J., Zhou, M., et al. 2017, *JGRA*, 122, 2024  
 Le, A., Egedal, J., Ohia, O., et al. 2013, *PhRvL*, 110, 135004  
 Le, A., Stanier, A., Daughton, W., et al. 2019, *PhPI*, 26, 102114  
 Lepping, R. P., & Behannon, K. W. 1980, *JGR*, 85, 4695  
 Lindqvist, P. A., Olsson, G., Torbert, R. B., et al. 2016, *SSRv*, 199, 137  
 Liu, Y. H., Hesse, M., Guo, F., et al. 2017, *PhRvL*, 118, 085101  
 Liu, Y. H., Hesse, M., Guo, F., et al. 2018, *PhPI*, 25, 080701  
 Mozer, F. S., Bale, S. D., & Phan, T. D. 2002, *PhRvL*, 89, 015002  
 Nakamura, T. K. M., Genestreti, K. J., Liu, Y. H., et al. 2018, *JGRA*, 123, 9150  
 Øieroset, M., Phan, T. D., Fujimoto, M., et al. 2001, *Natur*, 412, 414  
 Phan, T. D., Drake, J. F., Shay, M. A., et al. 2007, *PhRvL*, 99, 255002  
 Pollock, C., Moore, T., Jacques, A., et al. 2016, *SSRv*, 199, 331  
 Pritchett, P. L. 2008, *JGRA*, 113, A06210  
 Pritchett, P. L., & Mozer, F. S. 2009, *JGRA*, 114, A11210  
 Russell, C. T., Anderson, B. J., Baumjohann, W., et al. 2016, *SSRv*, 199, 189  
 Schwartz, S. J. 1998, in *Analysis Methods for Multi-Spacecraft Data*, ed. G. Paschmann & P. Daly (Noordwijk: ESA), 249  
 Shay, M. A., Drake, J. F., & Swisdak, M. 2007, *PhRvL*, 99, 155002  
 Sonnerup, B. U. Ö., & Scheible, M. 1998, in *Analysis Methods for Multi-Spacecraft Data*, ed. G. Paschmann & P. Daly (Noordwijk: ESA), 185  
 Swisdak, M. 2016, *GeoRL*, 43, 43  
 Torbert, R. B., Burch, J. L., Phan, T. D., et al. 2018, *Sci*, 362, 1391  
 Webster, J. M., Burch, J. L., Reiff, P. H., et al. 2018, *JGRA*, 123, 4858  
 Wilder, F. D., Ergun, R. E., Burch, J. L., et al. 2018, *JGRA*, 123, 6533  
 Wilder, F. D., Ergun, R. E., Eriksson, S., et al. 2017, *PhRvL*, 118, 265101  
 Xiao, C. J., Wang, X. G., Pu, Z. Y., et al. 2007, *NatPh*, 3, 609  
 Zenitani, S., Hesse, M., Klimas, A., et al. 2011, *PhRvL*, 106, 195003  
 Zhong, Z. H., Tang, R. X., Zhou, M., et al. 2018, *PhRvL*, 120, 075101  
 Zhong, Z. H., Zhou, M., Huang, S. Y., et al. 2019, *GeoRL*, 46, 6248  
 Zhou, M., Ashour-Abdalla, M., Deng, X., et al. 2017, *JGRA*, 122, 9513  
 Zhou, M., Berchem, J., Walker, R. J., et al. 2018, *JGRA*, 123, 1834  
 Zhou, M., Deng, X., Tang, R., et al. 2014, *JGRA*, 119, 1541  
 Zhou, M., Deng, X. H., Li, S. Y., et al. 2009, *JGRA*, 114, A02216  
 Zhou, M., Deng, X. H., Zhong, Z. H., et al. 2019, *ApJ*, 870, 34  
 Zhou, M., Pang, Y., Deng, X. H., et al. 2011, *JGRA*, 116, A06222